CHAPTER FIVE
TEST STRUCTURE DEVELOPMENT

A steel plane frame, which served as an ESDM test structure, was designed and fabricated. The frame was designed such that it possessed certain geometric and dynamic characteristics which enabled ESDM evaluation. This chapter discusses test structure development including initial design using a commercial finite element software package and fabrication. Also, predicted and actual dynamic characteristics are discussed and compared.

Nomenclature

A_{b_t}	cross-sectional area of threaded part of bolt
A_{b_u}	cross-sectional area of unthreaded part of bolt
C_1	constant
C_2	constant
C_3	constant
C_{θ_1}	constant
C_{θ_2}	constant
C_{θ_3}	constant
d_b	bolt pitch diameter
d_c	arbitrary displacement
d_w	washer diameter
D_J	effective flexural rigidity of column or brace surface
D_w	flexural rigidity of base plate
E	column or brace modulus of elasticity
E_b	bolt modulus of elasticity
E_m	base plate modulus of elasticity
F_c	force
h_o	column height
h_1	brace height
k_b	bolt translational stiffness
k_B	combined bolt translational stiffness
k_c	translational stiffness associated with one bolted connection
k_{c_θ}	rotational stiffness associated with one bolted connection

k_m	stiffness associated with compressed region surrounding each bolted connection
k_s	aggregrate column/base plate/test stand translational stiffness
k_t	translational stiffness associated with threaded part of bolt
k_u	translational stiffness associated with unthreaded part of bolt
k_w	translational stiffness associated with welded connection between column and base plate
$\tilde{k}_J$	non-linear translational joint stiffness
$\tilde{k}_{J_\theta}$	non-linear rotational joint stiffness
k_{w_θ}	rotational stiffness associated with welded connection between column and base plate
k_θ	rotational stiffness
k_{B_θ}	combined bolt rotational stiffness
k_{S_θ}	aggregrate column/base plate/test stand rotational stiffness
l_{b_t}	length of threaded part of bolt
l_{b_u}	length of unthreaded part of bolt
l_m	base plate length
M	joint moment
M_c	moment
M_J	joint moment
P	joint force
P_J	joint force
r_c	distance
S	constant
S_w	constant
S_θ	constant
S_{w_θ}	constant
t_m	base plate thickness
w_o	column width
w_1	brace width
w_m	base plate width
x, y, z	spatial Cartesian coordinates; spatial Cartesian components
α	frustum angle
π	pi, 3.141…
θ_c	angle
θ_x	rotation about test structure x-axis
θ_y	rotation about test structure y-axis
θ_z	rotation about test structure z-axis
ν	Poissons ratio

Test Structure Design Criteria

As mentioned before, certain ESDM capabilities were experimentally evaluated; specifically, the ability to reconstruct velocity fields with in-plane large components parallel to a structure surface in the presence of small of-of-plane velocity components transverse to the surface was evaluated. Therefore, a test structure possessing certain geometric and dynamic characteristics permitting such an evaluation was required.

Before the design process was initiated, several design criteria were established which ensured that the test structure possessed the necessary geometric and dynamic characteristics which permitted ESDM evaluation. First, simple geometry was required for any design considered. Simple geometry allowed the construction of a correspondingly simple ESDM finite element mesh which described surface geometry. Second, symmetric geometry was mandated; such symmetry helped ensure easily controlled structure motions. Third, several flat, smooth, orthogonal, structure surfaces were required. These surfaces facilitated accelerometer and force transducer mounting, aided LDV velocity measurement and assisted ESDM velocity field reconstruction. Fourth, the ability to generate and precisely control structure motion in two orthogonal directions was mandated. Hence, two structure vibration modes were required: one mode corresponding to motion in a particular direction and the other mode corresponding to motion in another, orthogonal direction. Fifth, good separation between these modes and neighboring modes was required for precise motion control. Sixth, structure materials and fabrication techniques which exhibit linear properties were mandated so

that the linear relationship between excitation and velocity response, a fundamental assumption invoked by ESDM, was not violated.

Test Structure Design Process

Test frame design began with the selection of a steel plane frame as the basic test structure form. A steel plane frame was selected since it satisfies many of the aforementioned design criteria including simple geometry, symmetric geometry and a construction material which exhibits linear properties.

Two plane frame types were considered: 1) a Vierendeel truss[7], which is actually not a truss since it possesses rigid, not pinned joints, but is so termed in the literature, and 2) a portal arch; both frame types are shown in Fig. 18. Both frames, when fixed at each

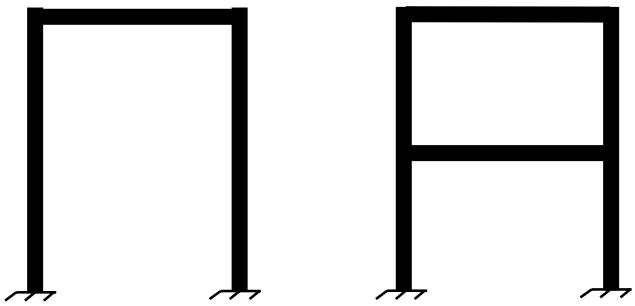

Figure 18. Portal arch and Vierendeel truss

column base, possess two vibration modes, first and second mode specifically, which correspond to out-of-plane and in-plane frame motions as illustrated by Fig. 19 for a Vierendeel truss. Hence, motion in two orthogonal directions may be generated with either type structure. However, based upon guidance provided by Mitchell [47],

[7] Vierendeel trusses were first proposed by a Belgian engineer, Arthur Vierendeel, in 1896 [48].

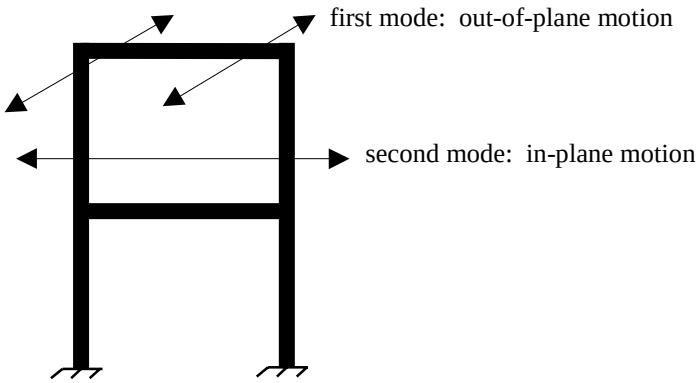

Figure 19. First and second mode motions exhibited by portal arches and Vierendeel trusses

Vierendeel trusses exhibit greater separation between first and second mode than portal arches of similar dimensions. Moreover, the separation between the first two modes and higher modes is greater. Therefore, Vierendeel truss motion is more precisely controlled than portal arch motion. Consequently, a Vierendeel truss was selected as the base test structure form.

Next, the following fabrication methods, ultimately incorporated into the final test structure design, were specified. First, rectangular hollow sections (RHS) composed of ASTM[8] A500 cold-rolled steel were specified for the frame columns and braces. The use of RHS ensured that the design criterion requiring several flat, orthogonal, smooth surfaces was satisfied. Second, 0.25 in. (6.3 mm) fillet welds were specified for all frame joints; bolts and press fits were discarded as possible attachment methods since loosening could occur over time, possibly introducing unwanted non-linear dynamic characteristics. Third, the following test structure/test stand attachment method was specified: two

[8] American Society of Testing and Materials, 100 Bar Harbor Drive, West Conshohocken, PA 19428

7.5x5.5x0.50 in. (190x140x13 mm) ASTM A36 steel plates centered and welded to the bottom of each frame column which, in turn, incorporate four symmetrically placed 0.5625 in. (14.29 mm) holes each for eight 0.50 in. (13 mm) coarse thread SAE[9] grade 5 bolts. The bolts secured the test structure to the test stand. This attachment method was dictated by the test stand which only allows bolted connections.

Last, member dimensions, including column and brace sizes and lengths, were determined using I-DEAS®, a mechanical engineering design, simulation and analysis software package developed and produced by the Structural Dynamics Research Corporation (SDRC)[10]. Several finite element models describing different test frame designs were constructed. Each test frame design specified different member dimensions, that is, different standard RHS sizes and lengths. Then, modal analysis results for each model were obtained and analyzed. Subsequently, based upon these results, a final design was selected. Specifically, the design alternative which possessed 1) the greatest separation between first and second mode and 2) the greatest separation between second and third mode was selected. Ultimately, a test structure with 3.0x3.0x0.25 in. (76x76x6.3 mm) RHS columns and 3.0x2.0x0.25 in. (76x51x6.3 mm) RHS braces was selected.

The next section discusses development of the test structure finite element models. Since this section contains much detail, the reader may want to continue directly to the subsequent section which fully describes the final test structure design.

[9] Society of Automotive Engineers, 400 Commonwealth Drive, Warrendale, PA 15096
[10] Structural Dynamics Research Corporation, 2000 Eastman Drive, Milford, OH 45150

Test Structure Finite Element Model Development

As mentioned previously, several finite element models, describing different test structure designs in terms of different RHS dimensions, were constructed. Each finite element model was constructed in the same manner.

All columns and braces were modeled by beam elements. The beam elements incorporated both rotary inertia and shear deformation effects. Typically, element lengths were approximately 1.0 in. (25 mm). Element nodes retained all six motion degrees-of-freedom: three translational motion degrees-of-freedom and three rotational motion degrees-of-freedom. Element cross-sectional geometric properties were determined by simply specifying cross-sectional shape and dimensions; required cross-sectional properties, such as area and area moments of inertia, were then automatically calculated by I-DEAS®. Additionally, from the cross-sectional geometry, I-DEAS® determined correction factors which permitted calculation of the appropriate element torsional stiffness. Cross-sectional shape was always a rectangular hollow section and cross-sectional dimensions corresponded to standard RHS sizes.

Welded frame joints between columns and braces were not assumed to be rigid. In an attempt to model welded joint stiffness, one-dimensional spring elements were used. Specifically, at each frame joint, spatially coincident beam element nodes were connected by three translational and three rotational spring elements. Each spring element required a stiffness value. Therefore, an extensive literature search was conducted to obtain a method for estimating translational and rotational joint stiffness between welded RHS. Two particularly appropriate methods described by Shehata,

Korol and Mirza [49] and Czechowski, Kordjak and Bródka [50] were discovered; the former method described by Shehata *et al*. is more recent and was selected for this work. Figure 20 illustrates a welded RHS joint. Figure 21 shows the corresponding stiffness model. Shehata *et al*. list two expressions which estimate the translational and rotational

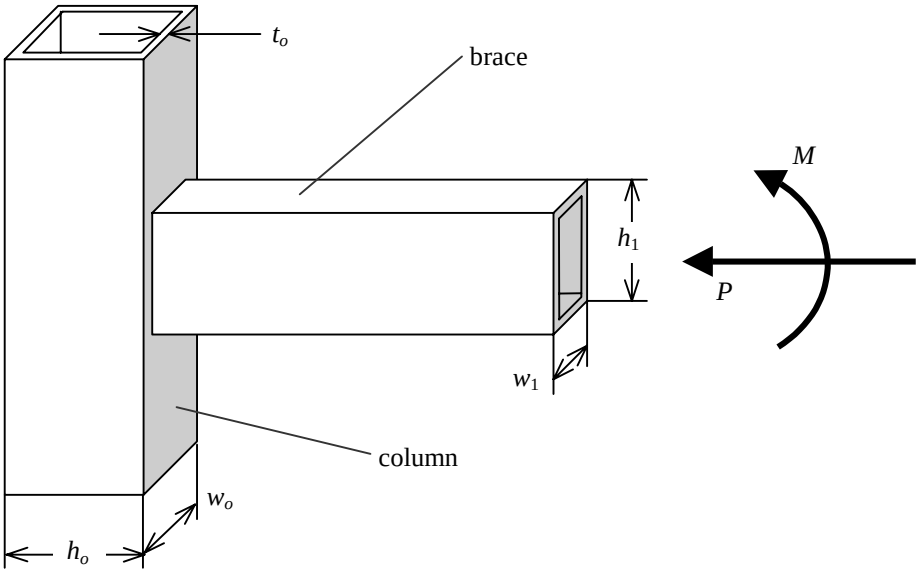

Figure 20. Welded RHS joint

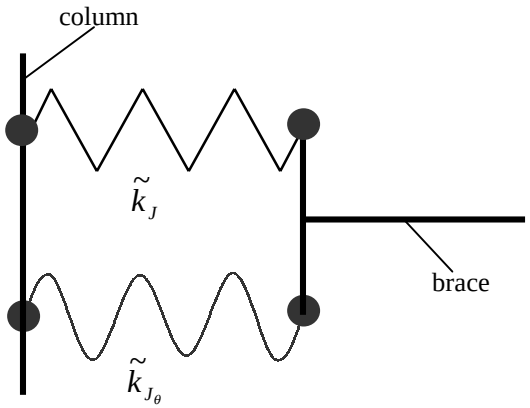

Figure 21. Stiffness model for welded RHS joint

stiffness associated with this type of joint. The expressions were developed by Shehata [51] and are based upon results obtained from finite element models originally developed by Korol and Mirza [52] which treat welded RHS joints as a distributed point load on a discretized plate. Considering Figs. 20 and 21, the expression for the translational joint stiffness, $\tilde{k}_J$, is

$$\tilde{k}_J = \frac{D_J}{w_o S}\left[C_1 + 3C_2\left(\frac{w_o S_\theta P_J}{D_J}\right)^2 + 5C_3\left(\frac{w_o S_\theta P_J}{D_J}\right)^4\right]^{-1}, \tag{118}$$

where D_J, the flexural rigidity of a plate with thickness t_o, is

$$D_J = \frac{E t_o^3}{12\left(1-\nu^2\right)} \tag{119}$$

and S is a factor defined by

$$S = \left(\frac{w_1}{w_o S}\right)^{\left(-0.67-9.62\frac{w_1}{w_o}\right)}\left(\frac{w_1}{h_1}\right)^{\left(1.17-1.05\frac{w_1}{h_1}\right)}\left(\frac{w_1}{t_o}\right)^{\left(-0.5-0.0008\frac{w_1}{t_o}\right)}. \tag{120}$$

Again considering Figs. 20 and 21, the expression for the rotational joint stiffness, $\tilde{k}_{J_\theta}$, is

$$\tilde{k}_{J_\theta} = \frac{D_J}{S_\theta}\left[C_{\theta_1} + 3C_{\theta_2}\left(\frac{S_\theta M_J}{D_J}\right)^2 + 5C_{\theta_3}\left(\frac{S_\theta M_J}{D_J}\right)^4\right]^{-1}, \tag{121}$$

where S_θ is

$$S_\theta = \left(\frac{w_1}{w_o}\right)^{\left(0.27-7.77\frac{w_1}{w_o}\right)}\left(\frac{w_1}{h_1}\right)^{\left(0.95-0.086\frac{w_1}{h_1}\right)}\left(\frac{w_1}{t_o}\right)^{\left(-0.45-0.0022\frac{w_1}{t_o}\right)}. \tag{122}$$

Equations (118) and (121) become highly non-linear for large brace axial forces, P_J, and moments, M_J; however, such high forces and moments were not expected since

only low test structure excitation force levels were anticipated. Evaluating Eq. (118) as P_J approaches zero yields

$$k_J = \lim_{P_J \to 0} \tilde{k}_J = \lim_{P_J \to 0} \frac{D_J}{w_o S}\left[C_1 + 3C_2\left(\frac{w_o S_\theta P_J}{D_J}\right)^2 + 5C_3\left(\frac{w_o S_\theta P_J}{D_J}\right)^4\right]^{-1} = \frac{D_J}{w_o S} C_1 ; \quad (123)$$

likewise, evaluating Eq. (121) as M_J approaches zero yields

$$k_{J_\theta} = \lim_{M_J \to 0} \tilde{k}_{J_\theta} = \lim_{M_J \to 0} \frac{D_J}{S_\theta}\left[C_{\theta_1} + 3C_{\theta_2}\left(\frac{S_\theta M_J}{D_J}\right)^2 + 5C_{\theta_3}\left(\frac{S_\theta M_J}{D_J}\right)^4\right]^{-1} = \frac{D_J}{S_\theta} C_{\theta_1} . \quad (124)$$

Spring element stiffness values were specified by Eqs. (123) and (124). Specifically, at each welded joint between a column and brace, a translational stiffness was calculated via Eq. (123) and assigned to each translational spring element; similarly, a rotational stiffness was calculated via Eq. (124) and assigned to each rotational spring element.

Assigning each translational and rotational spring element the same translational and rotational stiffness value, respectively, implied that joint stiffness in each direction was equal; but, Eqs. (123) and (124) are only valid for translational and rotational stiffness in the *x*-direction and θ_z-directions, respectively, as defined by Fig. 22. The following sensitivity analysis was conducted to determine if this assumption affected modal results for the first three modes. First, for a representative finite element model at each welded joint between a column and brace, only the spring elements aligned with the *x*-direction were assigned stiffness values calculated from Eqs. (123). The remaining spring elements were assigned infinite stiffness values[11]. Then modal results were

[11] Infinite stiffness is the largest numerical stiffness value accepted by I-DEAS®: approximately 9×10^{34} lbf(in)$^{-1}$ for translational stiffness and approximately 9×10^{34} lbf·in(rad)$^{-1}$ for rotational stiffness.

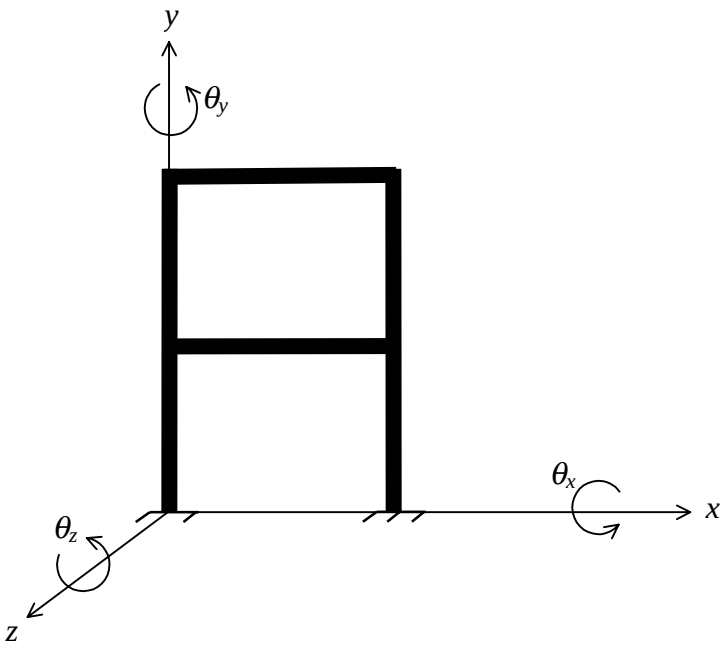

Figure 22. Test structure coordinate system

obtained. Second, this process was repeated for spring elements aligned with the remaining directions; translational and rotational stiffness values were calculated using Eqs. (123) and (124), respectively. Third, to simulate rigid joints, all spring elements in all directions were assigned infinite stiffness values and modal results obtained. Fourth, modal results for all three cases were compared. Modal results indicated that first, second and third mode are not affected by translational joint stiffness in any direction. Results also indicated that first, second and third mode are not affected by joint stiffness in the θ_x- and θ_y-directions. However, results indicated that second mode is affected by joint stiffness in the θ_z-direction; stiffness in this direction decreased second mode 42 Hz from 210 Hz for the rigid case. These results were expected since first and third mode all entail rotation about the test structure base in the θ_x-direction, not about the welded joints.

The exception is second mode which involves some rotation about the welded joints in the θ_z-direction. Therefore, at each joint between a column and brace, assigning all translational spring elements the same stiffness value obtained from Eq. (123) did not influence results for the first tree modes. In addition, assigning all rotational spring elements the same stiffness value obtained from Eq. (124) did not influence results for the first three modes.

Like the welded joints between columns and braces, the method used to attach the frame to the test stand was not considered rigid and six spring elements, three translational and three rotational elements, modeled the attachment locations at each column base. The actual attachment method for one base plate is shown in Fig. 23. Each

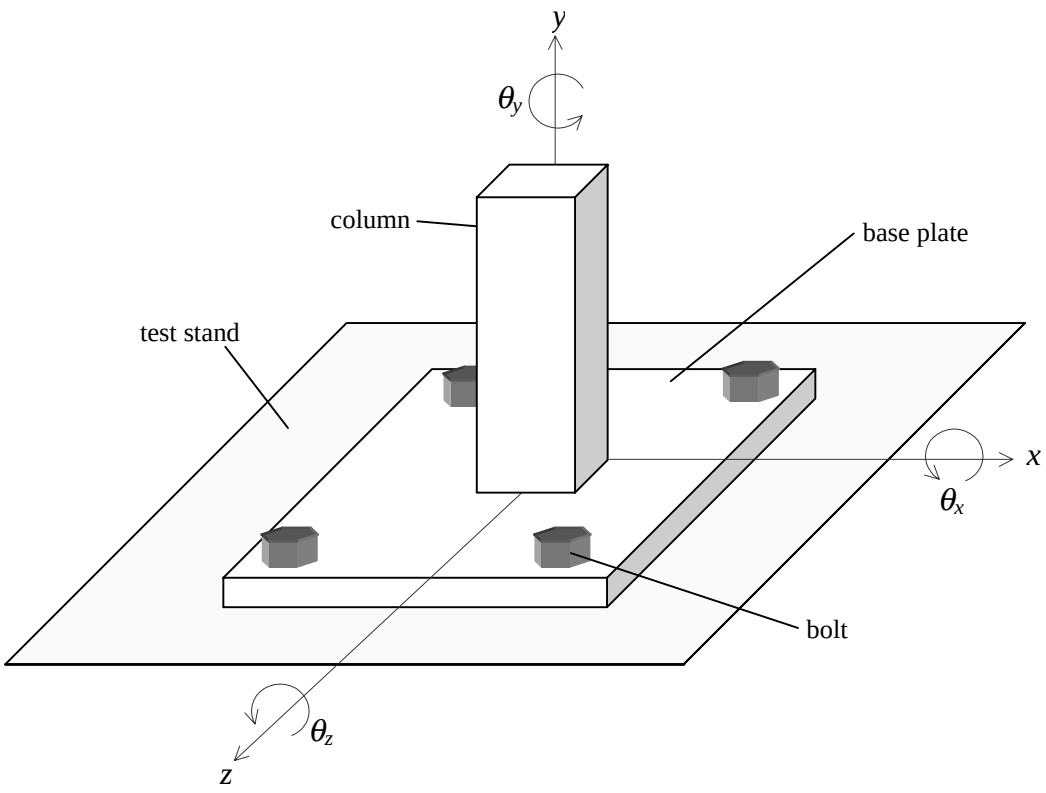

Figure 23. Base plate attachment method and coordinate

spring element was connected between spatially coincident beam element nodes and fixed ground nodes at each column base. The corresponding *y*-direction translational stiffness model is shown in Fig. 24. One spring modeled the welded connection stiffness

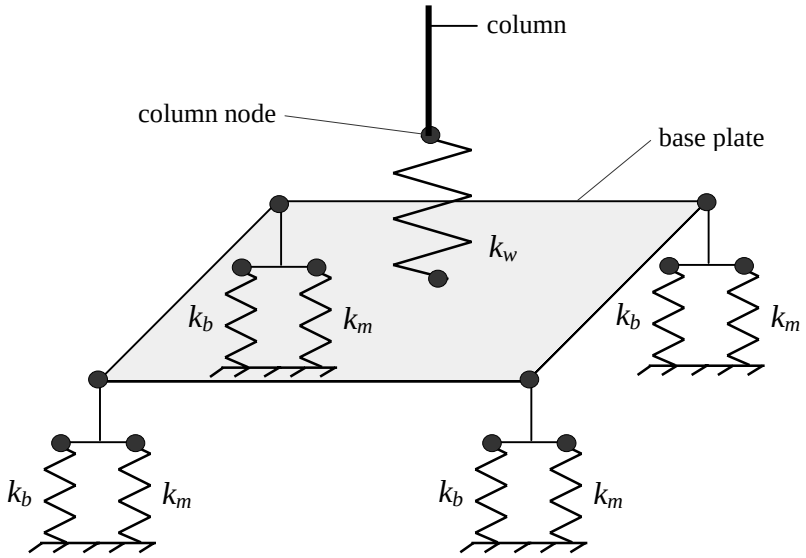

Figure 24. y-direction translational stiffness model for test stand attachment scheme

between each column and base plate and two springs in parallel modeled each bolted connection stiffness, four bolted connections for each plate. From a modified form of Eq. (123), an estimate of the welded connection stiffness is

$$k_w = \frac{D_w}{S_w} C_1, \tag{125}$$

where

$$D_w = \frac{E t_m^3}{12\left(1-\nu^2\right)} \tag{126}$$

and

$$S_w = \left(\frac{w_o}{w_m}\right)^{\left(-0.67-6.62\frac{w_o}{w_m}\right)}\left(\frac{w_o}{h_o}\right)^{\left(1.17-1.05\frac{w_o}{h_o}\right)}\left(\frac{w_o}{t_m}\right)^{\left(-0.5-0.0008\frac{w_o}{t_m}\right)}. \quad (127)$$

For each bolted connection, one spring modeled axial bolt stiffness, itself modeled by two series springs for the threaded and unthreaded bolt portions, and the other spring modeled stiffness associated with the compressed plate region surrounding the bolt. The axial bolt stiffness is

$$k_b = \frac{k_t + k_u}{\left(k_t + k_u\right)}, \quad (128)$$

where the stiffness of the threaded part is

$$k_t = \frac{A_{b_t} E_b}{l_{b_t}} \quad (129)$$

and the stiffness of the unthreaded part is

$$k_u = \frac{A_{b_u} E_b}{l_{b_u}}. \quad (130)$$

From Shigley and Mitchell [53], an expression that estimates stiffness associated with the compressed region surrounding each bolt is

$$k_m = \pi E_m d_b \tan\alpha \left\{ \ln\left[\frac{\left(2t_m \tan\alpha + d_w - d_b\right)\left(d_w + d_b\right)}{\left(2t_m \tan\alpha + d_w + d_b\right)\left(d_w - d_b\right)} \right] \right\}^{-1}, \quad (131)$$

where α =30°. Combining k_b and k_m in parallel yields the stiffness associated with one bolted connection:

$$k_c = k_b + k_m. \quad (132)$$

Each base plate has four bolted connections; these connections were modeled as four springs acting in parallel. Consequently, the stiffness associated with all four bolted connections for each base plate is

$$k_B = 4k_c \,. \tag{133}$$

Therefore, the *y*-direction translational stiffness associated with the test structure/test frame attachment scheme at each column base is the following series combination of the weld connection stiffness given by Eq. (125) and the aggregate bolted connection stiffness specified by Eq. (133):

$$k_s = \frac{k_w k_B}{k_w + k_B} \,. \tag{134}$$

Rotational stiffness associated with the test structure/test stand attachment scheme was also modeled; specifically, considering Fig. 23, rotational stiffness in the θ_x- and θ_z-directions was modeled. The rotational stiffness model for both directions is shown in Fig. 25. One spring modeled the welded connection rotational stiffness and four additional springs in parallel modeled each bolted connection rotational stiffness. Using a modified form of Eq. (124), an estimate for the welded connection stiffness in the θ_x-direction is

$$k_{w_{\theta_x}} = \frac{D_w}{w_m S_{w_{\theta_x}}} C_{\theta_1} \,, \tag{135}$$

where

$$S_{w_{\theta_x}} = \left(\frac{w_o}{l_m}\right)^{\left(0.27-7.77\frac{w_o}{l_m}\right)} \left(\frac{w_o}{h_o}\right)^{\left(0.95-0.086\frac{w_o}{h_o}\right)} \left(\frac{w_o}{t_m}\right)^{\left(-0.45-0.0022\frac{w_o}{t_m}\right)}; \tag{136}$$

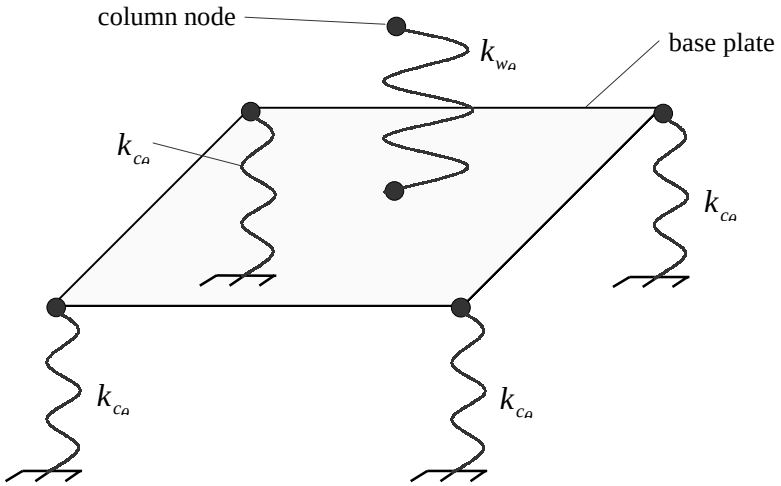

Figure 25. θ_x- and θ_z-direction rotational stiffness model for test stand attachment scheme

welded connection stiffness in the θ_z-direction was estimated in a similar manner:

$$k_{w_{\theta_z}} = \frac{D_w}{w_m S_{w_{\theta_z}}} C_{\theta_1}, \tag{137}$$

where

$$S_{w_{\theta_z}} = \left(\frac{w_o}{w_m}\right)^{\left(0.27-7.77\frac{w_o}{w_m}\right)} \left(\frac{w_o}{h_o}\right)^{\left(0.95-0.086\frac{w_o}{h_o}\right)} \left(\frac{w_o}{t_m}\right)^{\left(-0.45-0.0022\frac{w_o}{t_m}\right)}. \tag{138}$$

Bolted connection stiffness in the θ_x- and θ_z-directions was estimated in the following manner. Considering Fig. 26, each bolted connection is located an equal distance, r_c, from the column center; therefore, the y-direction translational stiffness, k_c, associated with each bolted connection is located the same distance from the column center. Considering Fig. 27, which shows the stiffness model for one bolted connection, the force developed in k_c due to an arbitrary displacement, d_c, is

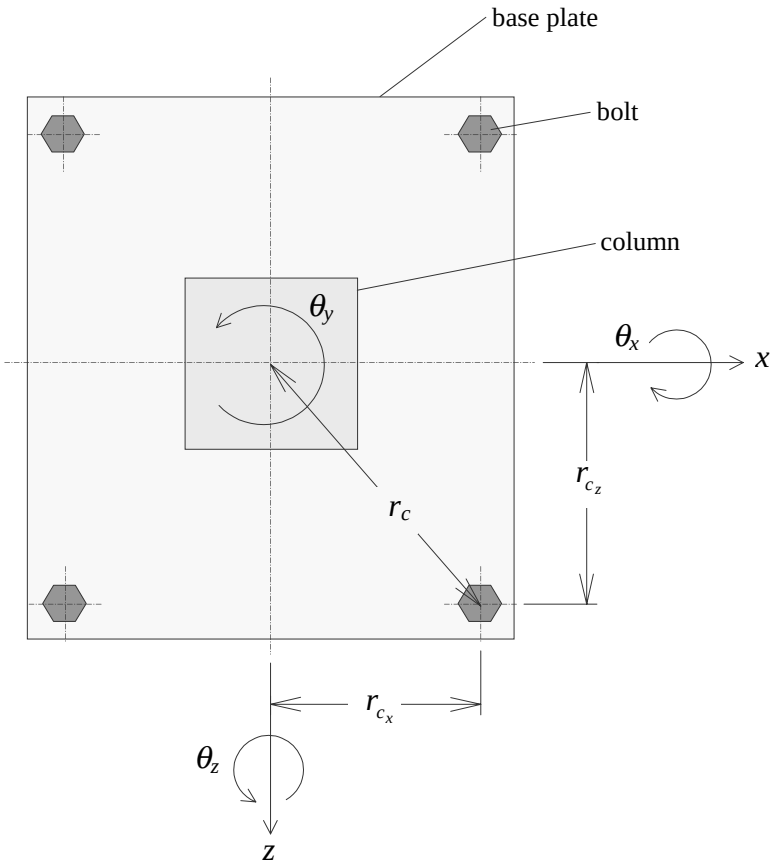

Figure 26. Plan view of test stand attachment scheme showing coordinate system and distances from arbitrary bolt to column center

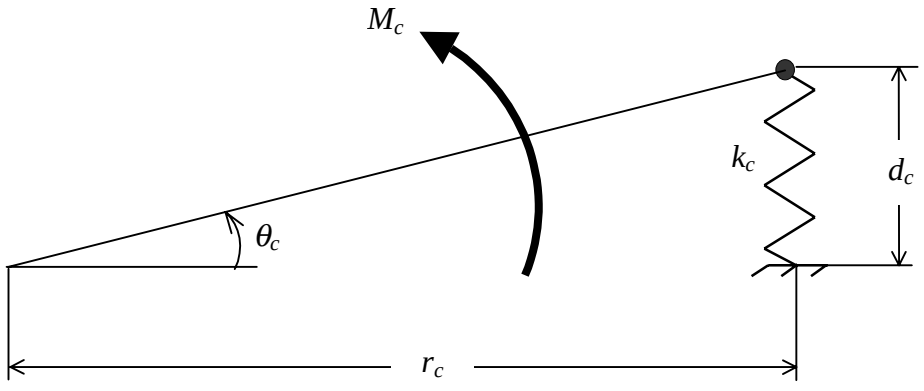

Figure 27. Model used to derive rotational stiffness associated with test stand attachment scheme

$$F_c = k_c d_c ; \tag{139}$$

Hence, the moment, M_c, developed at distance r_c by this force is

$$M_c = F_c r_c = k_c d_c r_c . \tag{140}$$

For small displacements d_c, the angle θ_c is

$$\theta_c = \frac{d_c}{r_c} . \tag{141}$$

In general, rotational stiffness is defined as

$$k_\theta \equiv \frac{M}{\theta} , \tag{142}$$

where M is an arbitrary moment and θ is the corresponding angular deflection. Therefore, the rotational stiffness associated with each bolted connection about the column center is

$$k_{c_\theta} = \frac{M_c}{\theta_c} = k_c r_c^2 , \tag{143}$$

Accordingly, the rotational stiffness components in the θ_x- and θ_z-directions are

$$k_{c_{\theta_x}} = k_c r_{c_x}^2 \tag{144}$$

and

$$k_{c_{\theta_z}} = k_c r_{c_z}^2 . \tag{145}$$

Then, the aggregate rotational stiffness for all four bolted connections in the θ_x-direction is

$$k_{B_{\theta_x}} = 4 k_{c_{\theta_x}} ; \tag{146}$$

in the θ_z-direction it is

$$k_{B_{\theta_z}} = 4k_{c_{\theta_z}}. \tag{147}$$

Combining the stiffness represented by Eqs. (135) and (146) in series yields the overall θ_x-direction rotational stiffness

$$k_{S_{\theta_x}} = \frac{k_{w_{\theta_x}} k_{B_{\theta_x}}}{k_{w_{\theta_x}} + k_{B_{\theta_x}}}. \tag{148}$$

Likewise, combining the stiffness represented by Eqs. (137) and (147) in series yields the overall θ_z-direction rotational stiffness

$$k_{S_{\theta_z}} = \frac{k_{w_{\theta_z}} k_{B_z}}{k_{w_{\theta_z}} + k_{B_z}}. \tag{149}$$

For each test structure/test stand attachment location at each column base, all translational springs were assigned the same translational stiffness value calculated using Eq. (134). Rotational spring elements aligned with the θ_x- and θ_z-directions were assigned rotational stiffness values calculated from Eqs. (148) and (149), respectively. The rotational spring element aligned with the θ_y-direction was arbitrarily assigned the same value as that for the θ_x-direction.

Again, a sensitivity analysis was conducted to determine if assigning each translational spring element the same translational stiffness value affected modal results for the first three modes. Modal results obtained from the sensitivity analysis indicated that the first three modes are relatively unaffected by translational stiffness associated with the test structure/test stand attachment scheme. Moreover, results indicated that first, second and third mode are not affected by rotational stiffness in the θ_y-direction. However, rotational stiffness aligned with the θ_x- and θ_z-directions greatly affected

second and first mode results, respectively. The computed stiffness in the θ_x-direction decreased first mode 87 Hz from 208 Hz for the rigid case and stiffness in the θ_z-direction decreased second mode 59 Hz from 227 Hz for the rigid case. Again, these results were expected since first and second modes entail rotation about the test structure base in the θ_x- and θ_z-directions, respectively. Therefore, assigning each translational spring element the same stiffness value obtained from Eq. (134) did not affect results for the first three modes. Furthermore, arbitrarily assigning rotational spring elements aligned with the θ_y-direction the same stiffness value as those elements aligned with the θ_x-direction did not affect results for the first three modes.

Final Test Structure Design

Modal results were obtained after each finite element model, which described each test structure design alternative in terms of different RHS dimensions, was constructed. These results were then compared. Subsequently, as indicated before, a final design was selected which provided 1) the greatest separation between first and second mode and 2) the greatest separation between second and third mode.

Figure 28 depicts the final test structure design selected. The frame is 24.0 in. (609 mm) high and 12.0 in. (305 mm) wide. Two standard 3.0x3.0x0.25 in. (76x76x6.3 mm) RHS form the columns and two standard 3.0x2.0x0.25 in. (76x51x6.3 mm) RHS form the braces. As mentioned before, the braces are welded to the columns with 0.25 in. (6.3 mm) filet welds. Two 7.5x5.5x0.50 in. (190x140x13) mm steel plates welded to the bottom of each column with 0.25 in. (6.3 mm) filet welds provide frame base support. The plates each have four 0.5625 in. (14.29 mm) diameter holes for attachment to the

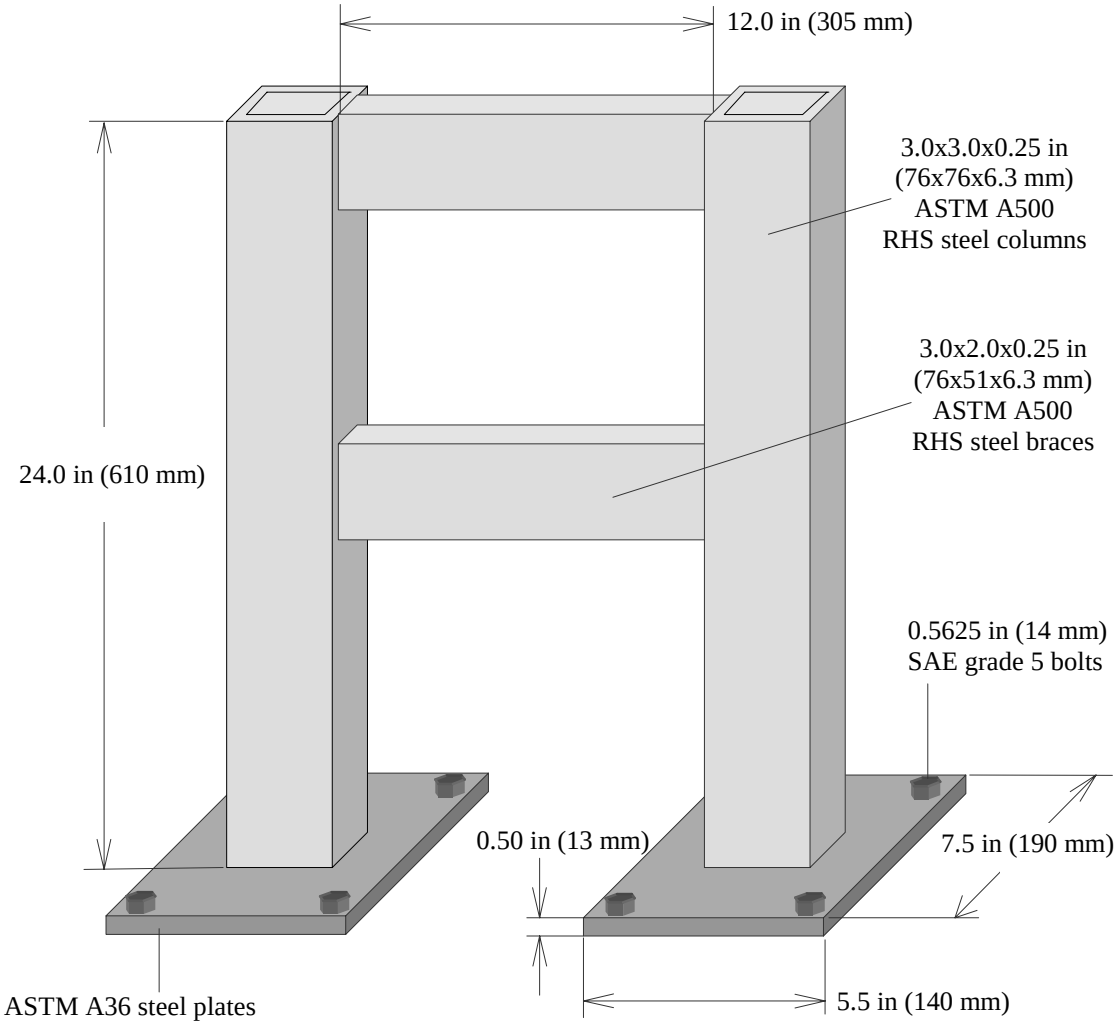

Figure 28. Final test structure design

rigid laboratory test stand with eight 0.50 in. (13 mm) diameter coarse thread SAE grade 5 steel bolts, four bolts for each plate.

Predicted modal characteristics for this design are listed in Table 5. Other designs possessed greater separation between first and second mode and second and third mode individually; however, the final design possessed the greatest separation between each of these modes collectively.

Table 5. Predicted test structure modal characteristics

Mode	Natural Frequency (Hz)	Mode Shape
1	121	pure out-of-plane motion: 
2	168	pure in-plane motion: 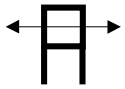
3	319	twisting about line of symmetry: 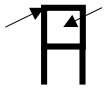

Mode shapes were obtained by animating modal results in I-DEAS®. First and second mode animations indicated flexible out-of-plane and in-plane frame motion about the ground attachment locations at each column base. Frame motion at first and second mode was uniform and no individual column or brace motion was visually detected. Third mode involved twisting of the frame about its axis of symmetry as shown in Table 5; hence, brace motion was visible.

Second mode results listed in Table 5 are dependent upon rotational stiffness associated with welded joints between columns and braces in the θ_z-direction specified by Fig. 22. In addition, first, second and third mode results listed in Table 5 are dependent upon rotational stiffness associated with the base plate/test stand attachment scheme in the θ_x- and θ_z-directions as specified by Fig. 23. Therefore, for completeness, the stiffness values assigned to the translational spring elements which simulated welded joint and base plate/test stand translational stiffness in the finite element model for the

final design are listed in Table 6. Likewise, the stiffness values assigned to rotational spring elements are listed in Table 7.

Table 6. Stiffness values assigned to translational spring elements in finite element model for final test structure design

Direction	Stiffness Values Assigned to Translational Spring Elements lbf $(in)^{-1}$ $(N(m)^{-1})$	
	Welded Joints Between Braces and Columns	**Base Plate/Test Stand Attachment Scheme**
x	$1.18x10^6$ $(2.07x10^8)$	$1.97x10^6$ $(3.45x10^8)$
y	$1.18x10^6$ $(2.07x10^8)$	$1.97x10^6$ $(3.45x10^8)$
z	$1.18x10^6$ $(2.07x10^8)$	$1.97x10^6$ $(3.45x10^8)$

Table 7. Stiffness values assigned to rotational spring elements in finite element model for final test structure design

Direction	Stiffness Values Assigned to Rotational Spring Elements lbf·in$(rad)^{-1}$ $(N\cdot m(rad)^{-1})$	
	Welded Joints Between Braces and Columns	**Base Plate/Test Stand Attachment Scheme**
θ_x	$8.82x10^6$ $(9.97x10^5)$	$2.36x10^7$ $(2.67x10^6)$
θ_y	$8.82x10^6$ $(9.97x10^5)$	$2.36x10^7$ $(2.67x10^6)$
θ_z	$8.82x10^6$ $(9.97x10^5)$	$2.46x10^7$ $(2.78x10^6)$

Test Structure Fabrication

Once the final design was completed, the test structure was fabricated. From an assembly drawing which detailed the final design, fabrication was performed by local departmental machine shop personnel. All column and brace RHS were donated by the Welded Tube Corporation of America[12]. Once the test structure was fabricated, it was mounted on the laboratory test stand as pictured in Fig. 29. Based upon guidance

[12] Welded Tube Company of America, 1855 East 122nd Street, Chicago, IL 60633

provided by Mitchell [54] and a procedure outlined in Shigley and Mitchell [55], each mounting bolt was tightened with a calibrated torque wrench until the induced tensile stress approximately equaled eighty percent of the bolt proof strength. Steel washers were used with each bolt.

Figure 29. Test structure bolted to test stand

Actual Test Structure Modal Characteristics

After the test structure was mounted on the test stand, actual test structure modal characteristics were experimentally obtained. The test structure was excited with a Kistler[13] model 9724A2000 impact hammer. Simultaneously, test structure response was measured by a model 303AO2 accelerometer provided by PCB® Piezotronics[14]. As

[13] Kistler Instrument Corporation, 75 John Glenn Drive, Amherst, NY 14228
[14] PCB Piezotronics, Inc., 3425 Walden Avenue, Depew, NY 14043

depicted in Fig. 30, the accelerometer was mounted with accelerometer wax to the top surface center of the top test structure brace. Impact hammer force and accelerometer acceleration data were acquired and processed using a Hewlett-Packard[15] model 35665A digital signal analyzer.

Experimental modal results were obtained for the following cases. First, as shown in Fig. 30, the accelerometer was oriented to measure *z*-direction, or out-of-plane, acceleration. Then the test structure was struck five times by the impact hammer in the *z*-

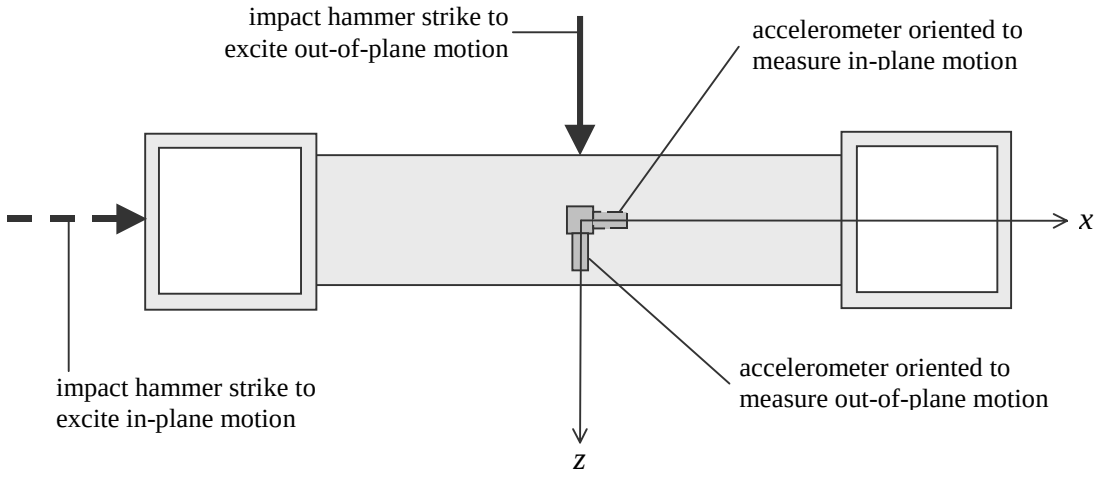

Figure 30. Plan view of test structure showing accelerometer placement and impact hammer strike locations

direction on the top brace side surface. Striking the test structure in this manner excited first mode. Figures 31 and 32 show averaged mobility magnitude and phase, respectively, and Fig. 33 shows coherence. First mode is located near 103 Hz. This result is 18 Hz lower than the predicted value of 121 Hz listed in Table 5.

[15] Hewlett-Packard, Inc., 8600 Soper Hill Road, Everett, WA 98205

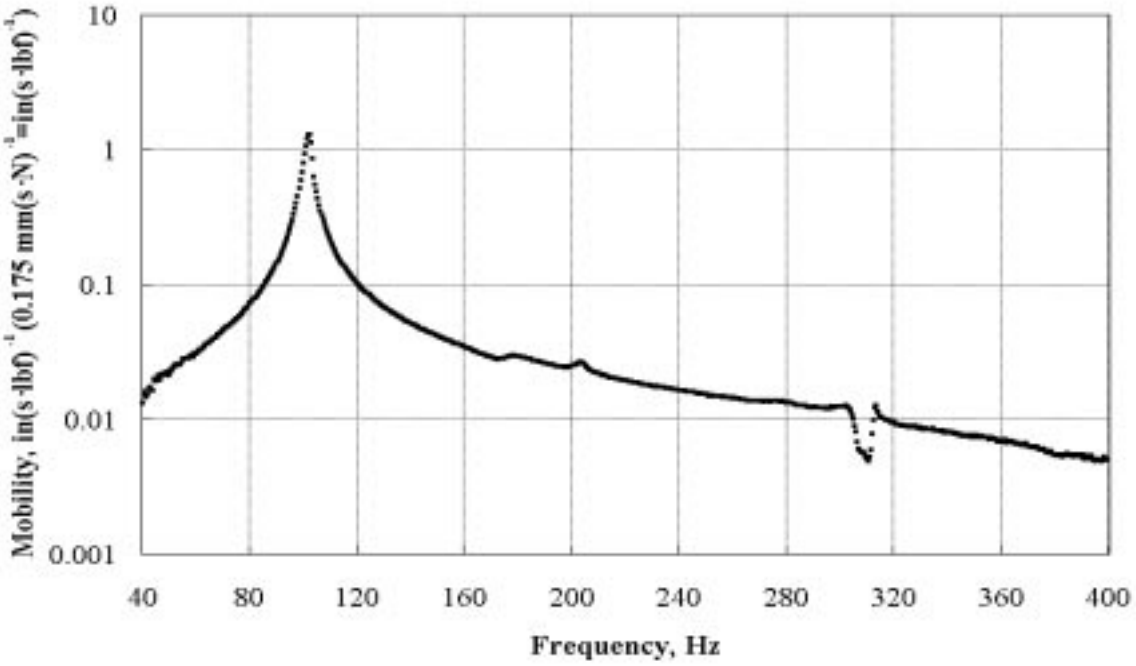

Figure 31. Mobility magnitude: out-of-plane excitation and response

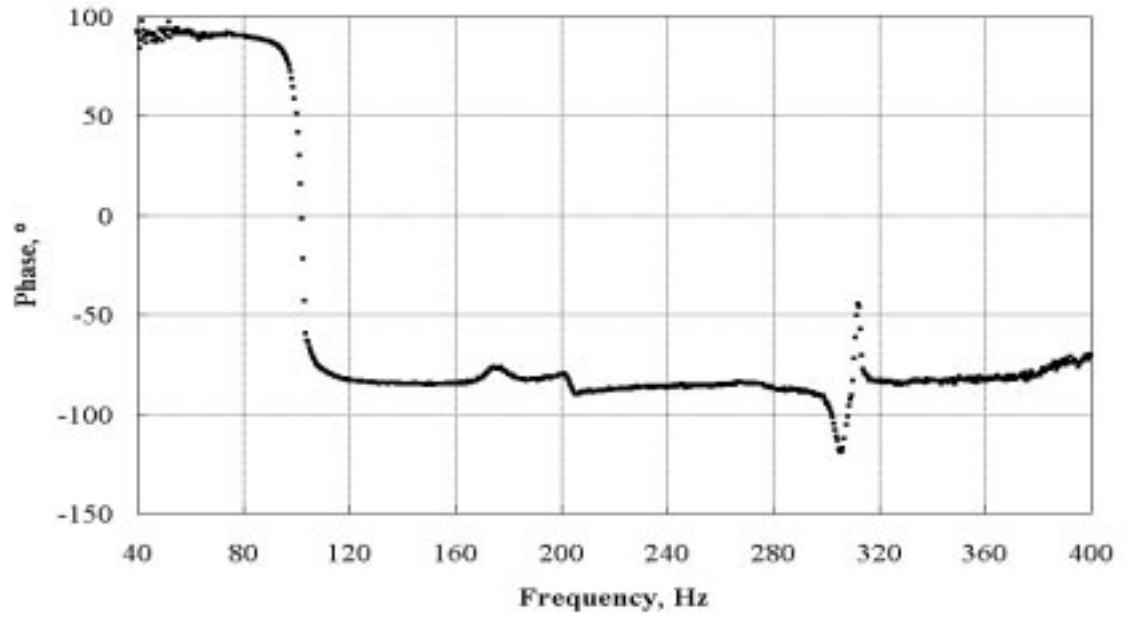

Figure 32. Mobility phase: out-of-plane excitation and response

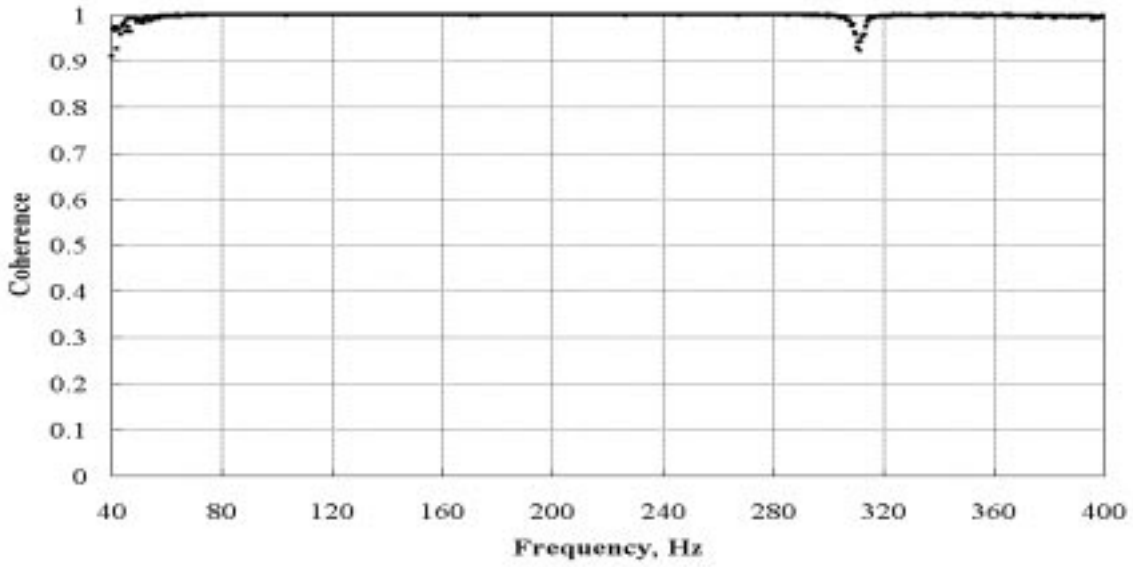

Figure 33. Coherence: out-of-plane excitation and response

Second, again considering Fig. 30, accelerometer orientation was maintained in the *z*-direction and the test structure was struck five times in the in the *x*-direction at the center of the column side surface near the column top exciting second mode. Figures 34 and 35 show averaged mobility magnitude and phase and Fig. 36 shows coherence.

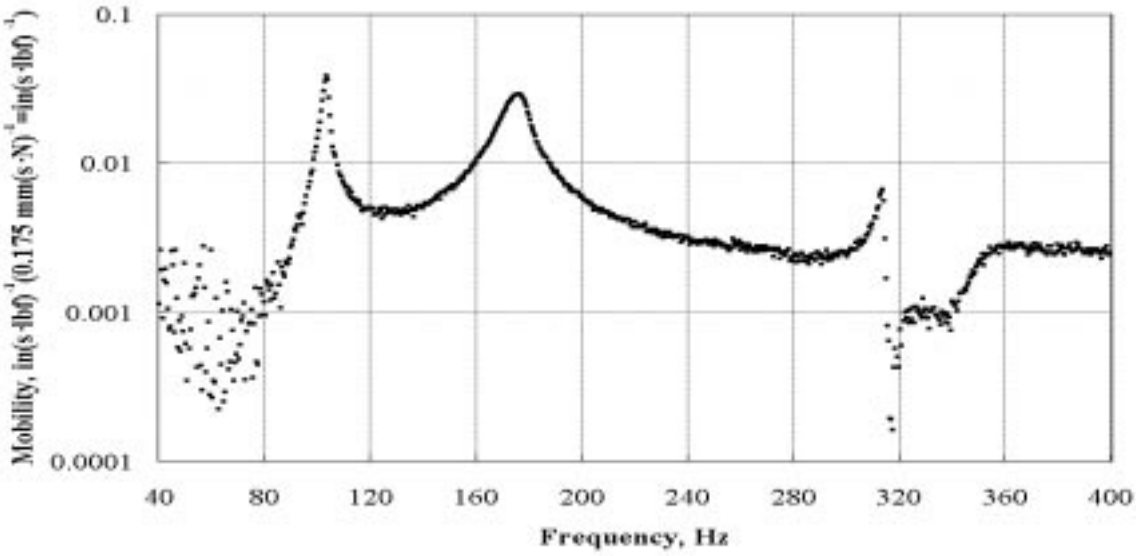

Figure 34. Mobility magnitude: in-plane excitation and out-of-plane response

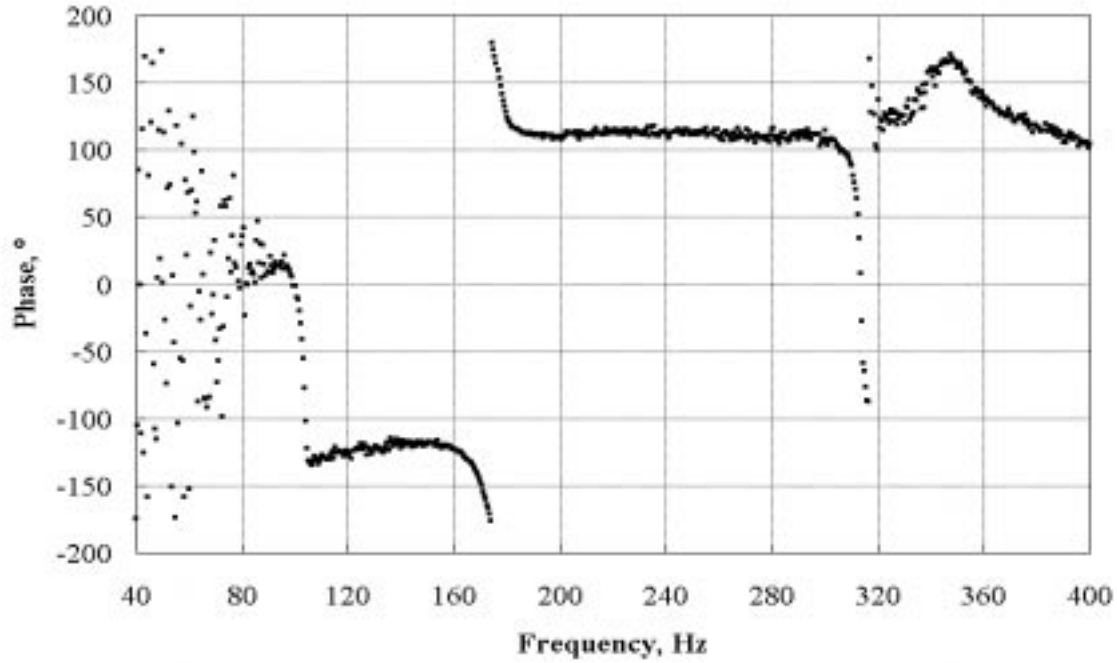

Figure 35. Mobility phase: in-plane excitation and out-of-plane response

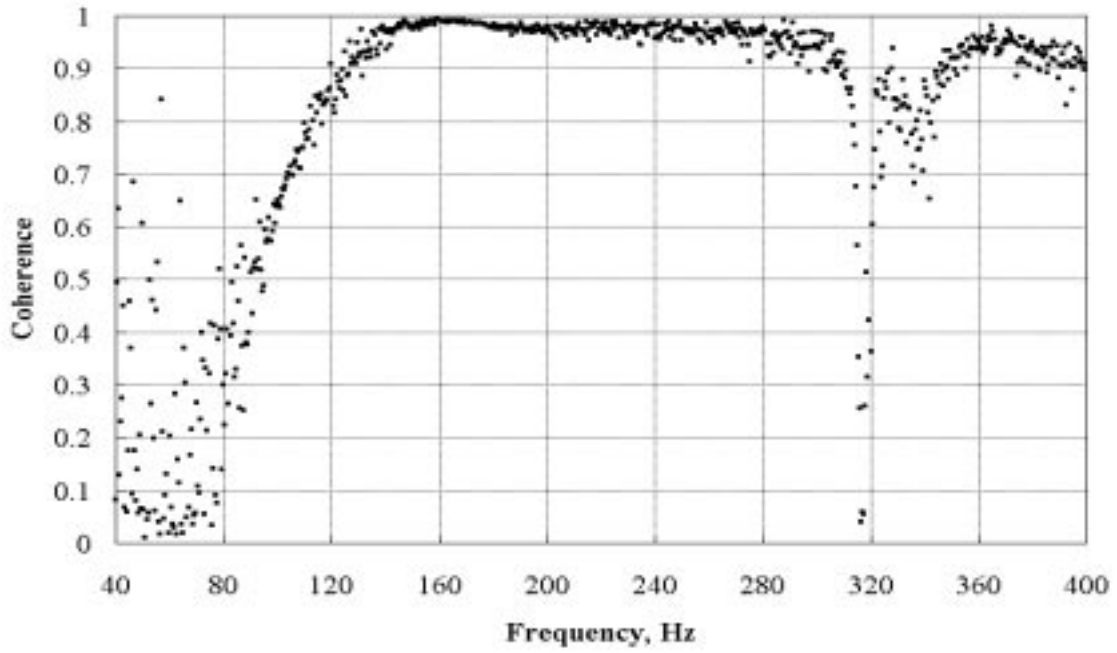

Figure 36. Coherence: in-plane excitation and out-of-plane response

Third, considering Fig. 30 again, the accelerometer was oriented to measure *x*-direction, or in-plane, acceleration. Then the test structure was struck five times by the impact hammer in the *x*-direction at the center of the column side surface near the column top. Striking the test structure in this manner excited second mode. Figures 37 and 38 show averaged mobility magnitude and phase, respectively, and Fig. 39 shows coherence. Second mode is located near 176 Hz. The response at third mode, approximately 320 Hz, was probably caused by impact hammer strikes not perfectly parallel to the *x*-direction. Such misalignment induced third mode motion. These results closely agree with the finite element model results listed in Table 5 which predicted second and third mode at 168 Hz and 319 Hz, respectively.

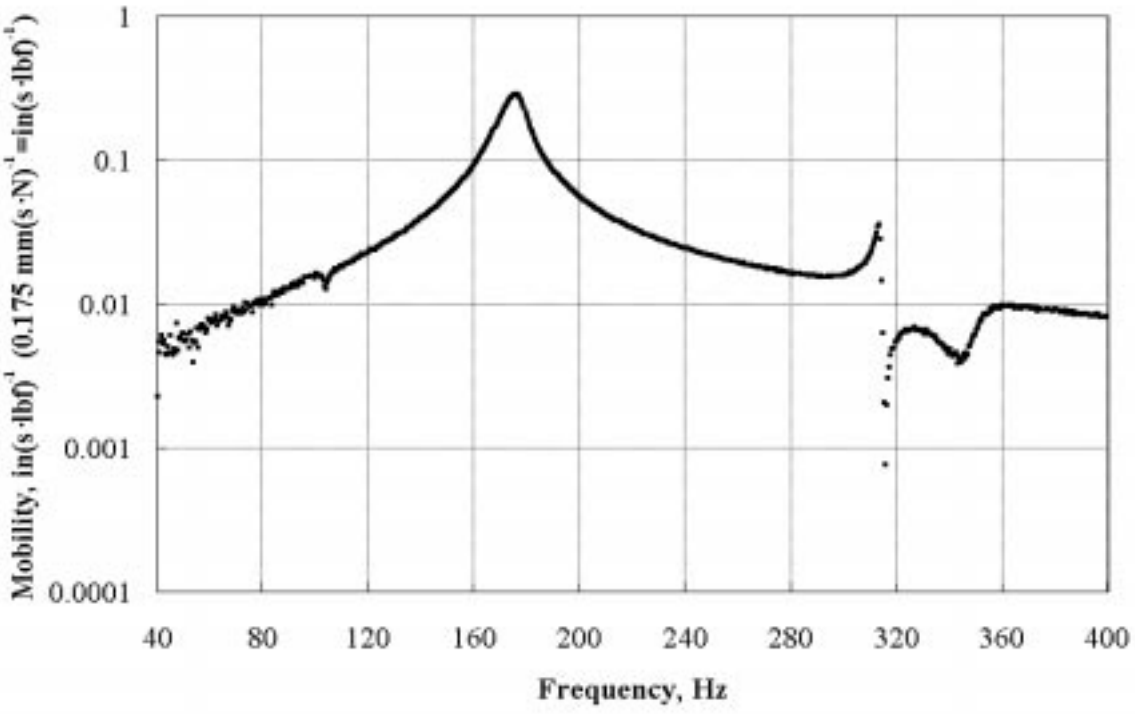

Figure 37. Mobility magnitude: in-plane excitation and response

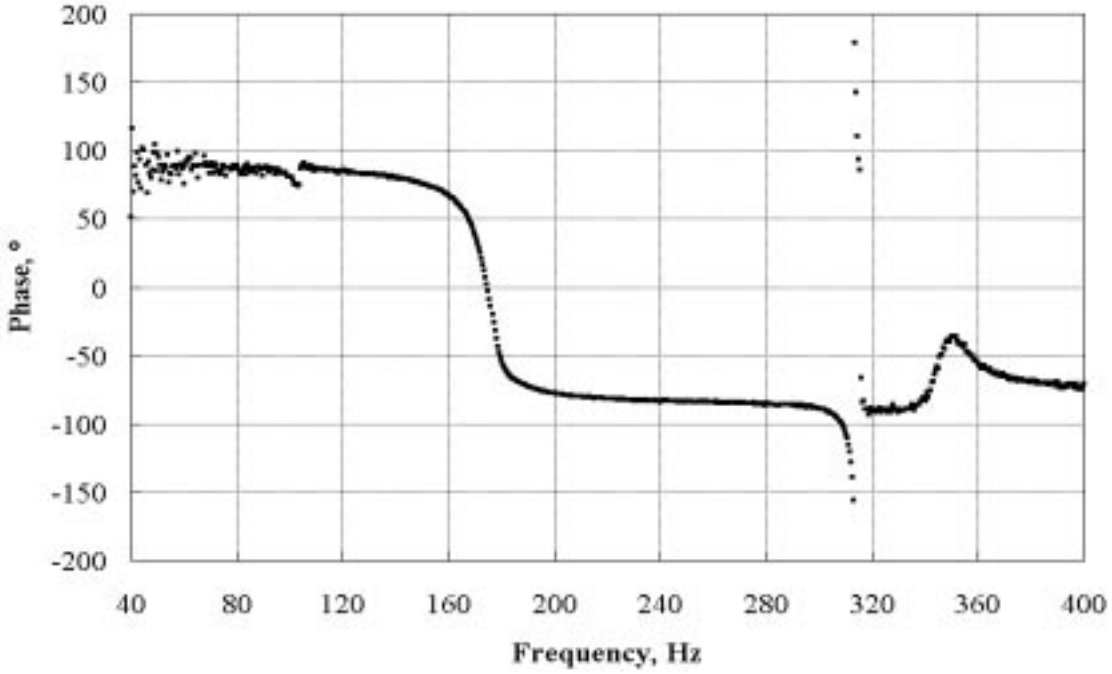

Figure 38. Mobility phase: in-plane excitation and response

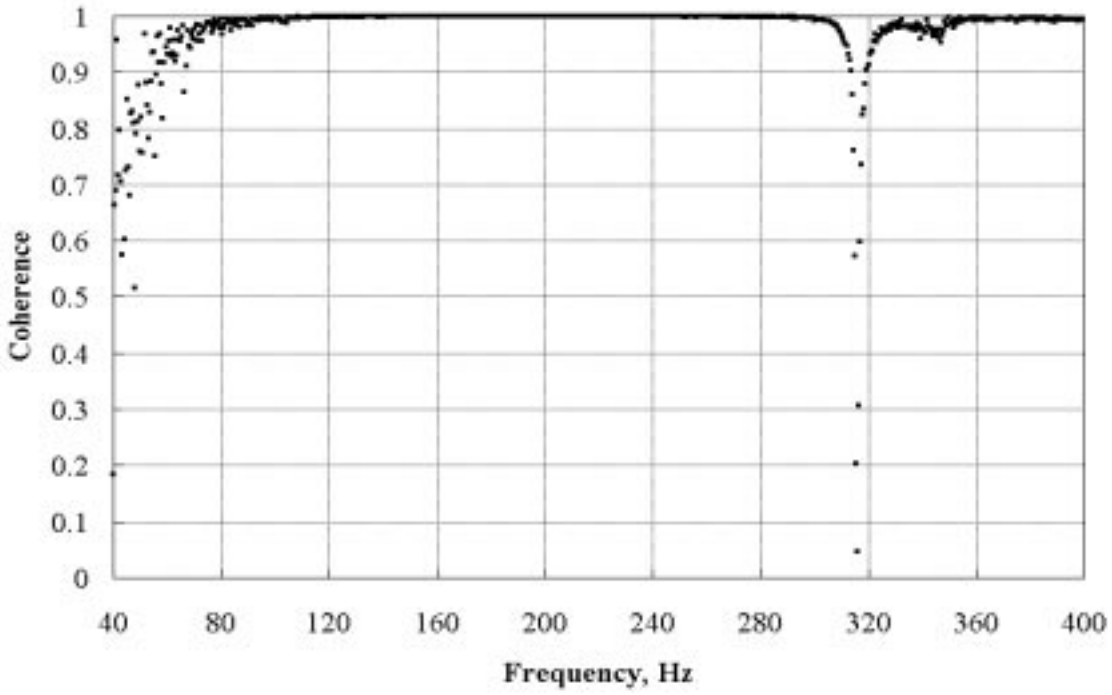

Figure 39. Coherence results: in-plane excitation and response

Fourth, again considering Fig. 30, accelerometer orientation was maintained in the *x*-direction and the test structure was struck five times by the impact hammer in the *z*-direction at the center of the top brace side surface, thus exciting second mode. Figures 40 and 41 show averaged mobility magnitude and phase and Fig. 42 shows coherence. An unexplained mode is present between second and third mode at 206 Hz.

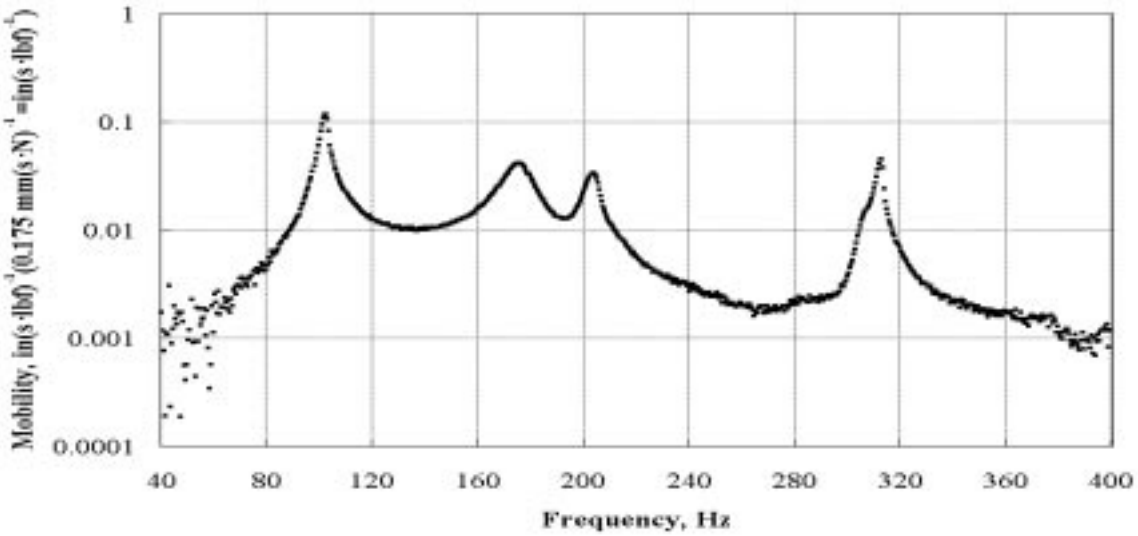

Figure 40. Mobility magnitude: out-of-plane excitation and in-plane response

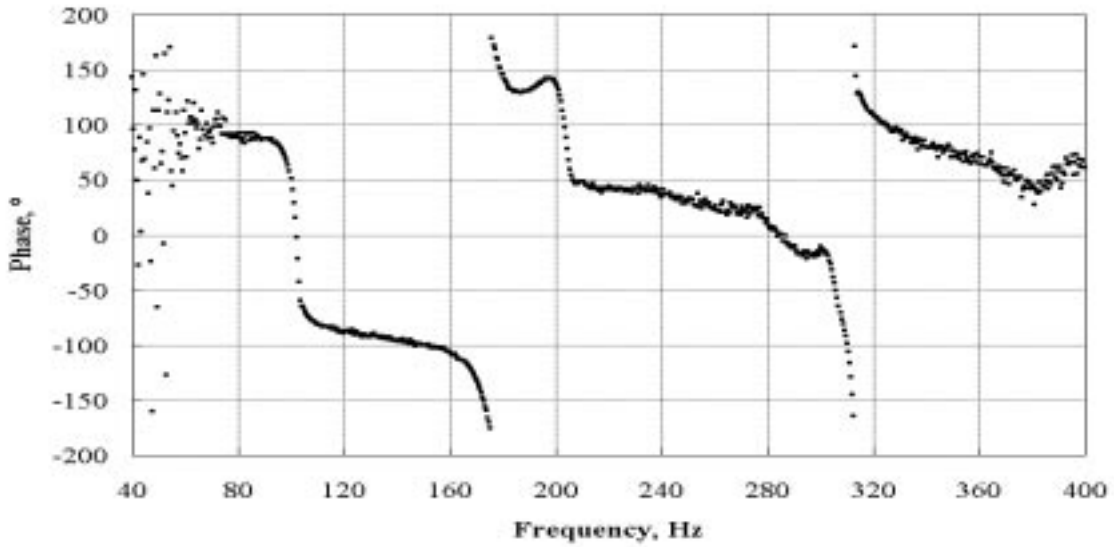

Figure 41. Mobility phase: out-of-plane excitation and in-plane response

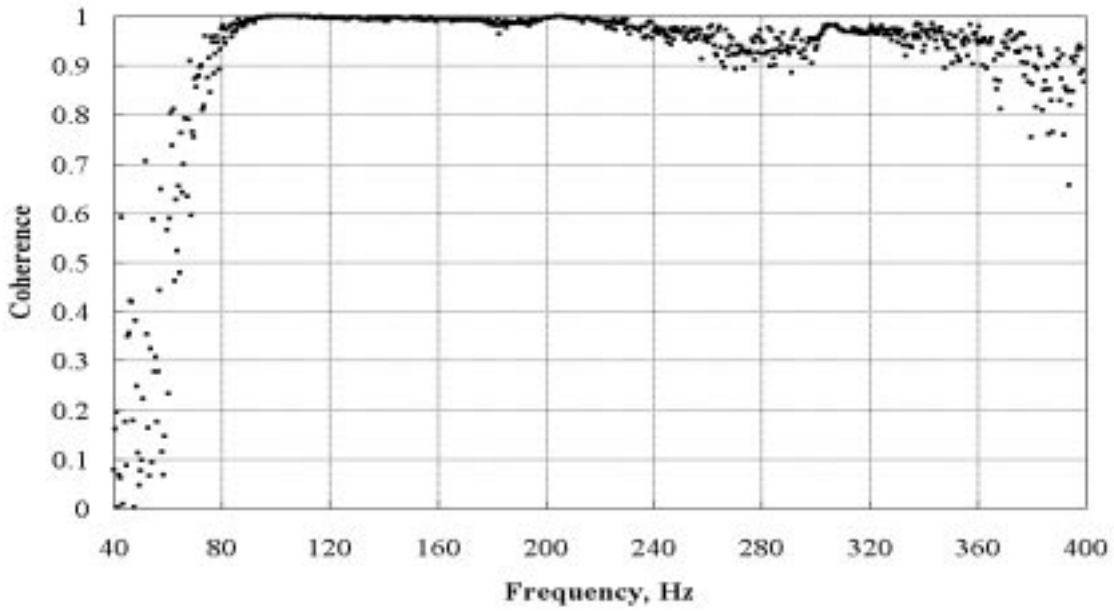

Figure 42. Coherence: in-plane excitation and out-of-plane response

From Fig. 31 the mobility magnitude at first mode is approximately 1.4 in(s·lbf)$^{-1}$ (8.0 mm(s·N)$^{-1}$); considering Fig. 40, the mobility magnitude at first mode is approximately 7.9% of this value, or 0.11 in(s·lbf)$^{-1}$ (0.63 mm(s·N)$^{-1}$). Also, from Fig. 37, the mobility magnitude at second mode is about 0.29 in(s·lbf)$^{-1}$ (1.7 mm(s·N)$^{-1}$); considering Fig. 34, the mobility magnitude at second mode is about 11% of this value, or 0.032 in(s·lbf)$^{-1}$ (0.18 mm(s·N)$^{-1}$). However, the maximum accelerometer transverse sensitivity is 1.8% [56]. Therefore, substantial in-plane motion was present when the test structure was struck in the *z*-direction and is unexplained by accelerometer transverse sensitivity. Similarly, substantial out-of-plane motion was present when the test structure was struck in the *x*-direction. Two explanations account for such phenomena. First, for each case, hammer strike misalignment imparted some in-plane and out-of-plane excitation, respectively. Second, geometric coordinate coupling caused by test structure

asymmetry probably exists. Hence, first and second mode motions are not pure out-of-plane and in-plane motions, respectively, as indicated by the finite element model.

A simple analysis was conducted to determine if first and second mode are pure out-of-plane and in-plane motions, respectively. As shown in Fig. 43, the accelerometer was oriented in several directions just off the *z*-axis and mobility results were recorded for hammer strikes in the *z*- and *x*-directions. Results obtained when the accelerometer was oriented about 5° from the z-axis indicate pure out-of-plane motion. Averaged mobility magnitude and phase for the *z*- and *x*-direction excitations are shown in Figs. 44 and 45, respectively. First mode magnitude is approximately 1.4 $in(s \cdot lbf)^{-1}$ (8.0

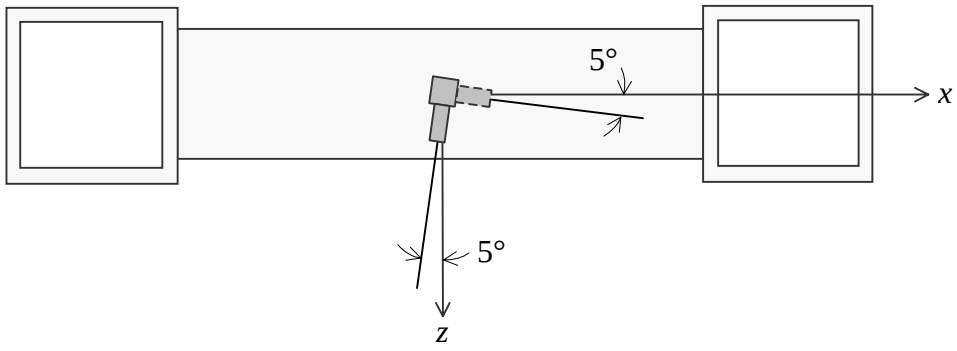

Figure 43. Plan view of test structure showing accelerometer placement and impact hammer strike locations

$mm(s \cdot N)^{-1}$) and 0.017 $in(s \cdot lbf)^{-1}$ (0.097 $mm(s \cdot N)^{-1}$) in Figs. 31 and 32, respectively. The percent ratio between these two values is 1.2%, below the maximum accelerometer transverse sensitivity. Thus, pure out-of-plane motion at first mode does not occur along the *z*-axis; however, pure first mode motion does occur along an axis oriented about 5° from the *z*-axis.

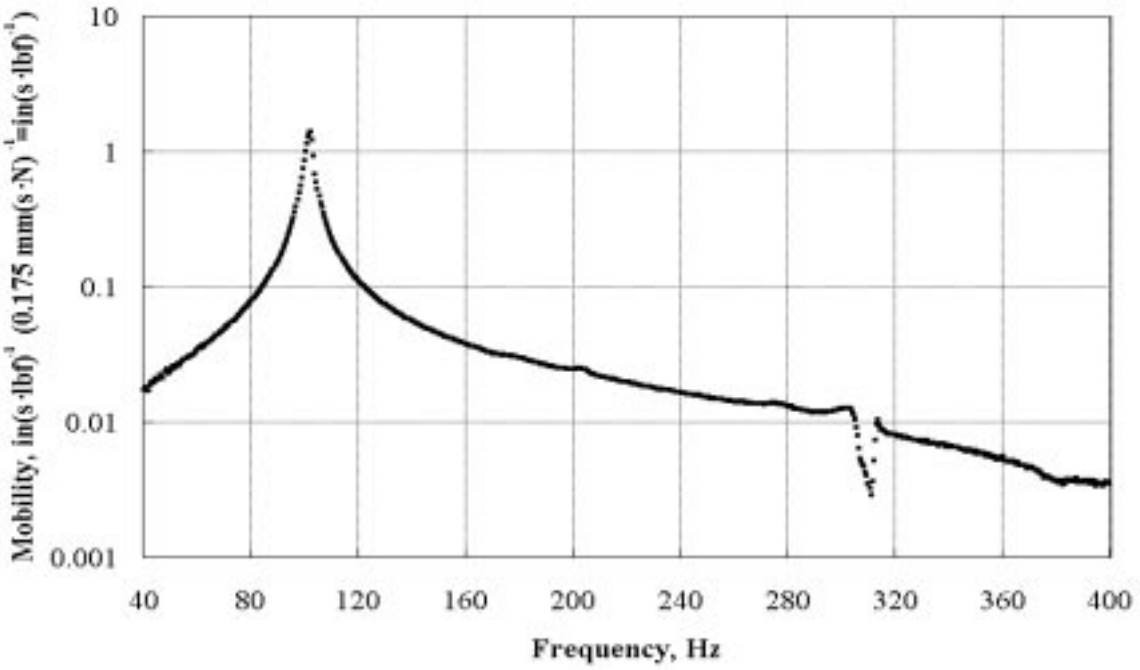

Figure 44. Mobility magnitude for out-of-plane excitation and response recorded along direction oriented about 5° from test structure *z*-axis

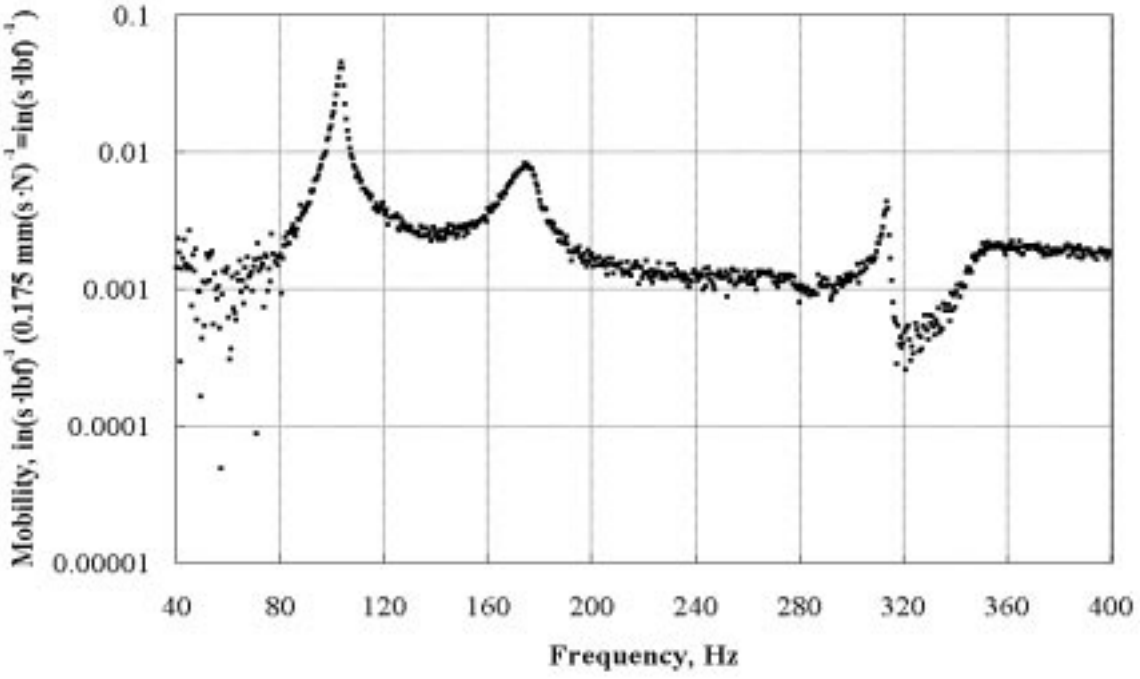

Figure 45. Mobility magnitude for in-plane excitation and out-of-plane response recorded along direction oriented about 5° from test structure *z*-axis

Since pure first mode motion was detected along an axis oriented about 5° from the test structure *z*-axis, it was reasoned that pure second mode motion should occur along an axis oriented about 5° from the test structure *z*-axis. Therefore, as shown in Fig. 43, the accelerometer was oriented about 5° from the *x*-axis. Mobility results were obtained for hammer strikes in the *x*- and *z*-directions. Averaged mobility magnitude for the *x*- and *z*-direction excitations are shown in Figs. 46 and 47, respectively. Second mode magnitude is approximately 0.27 in(s·lbf)$^{-1}$ (1.5 mm(s·N)$^{-1}$) and 0.0069 in(s·lbf)$^{-1}$ (0.039 mm(s·N)$^{-1}$) in Figs. 46 and 47, respectively. Again, an unexplained mode is present between second and third mode at 206 Hz. The percent ratio between these two values is 2.6%, still above the maximum accelerometer transverse sensitivity, but much lower than the original percent ratio value of 11%. Thus, pure in-plane motion at second mode does not occur along the *x*-axis; however, as reasoned, pure second mode motion does occur along an axis oriented approximately 5° from the *x*-axis.

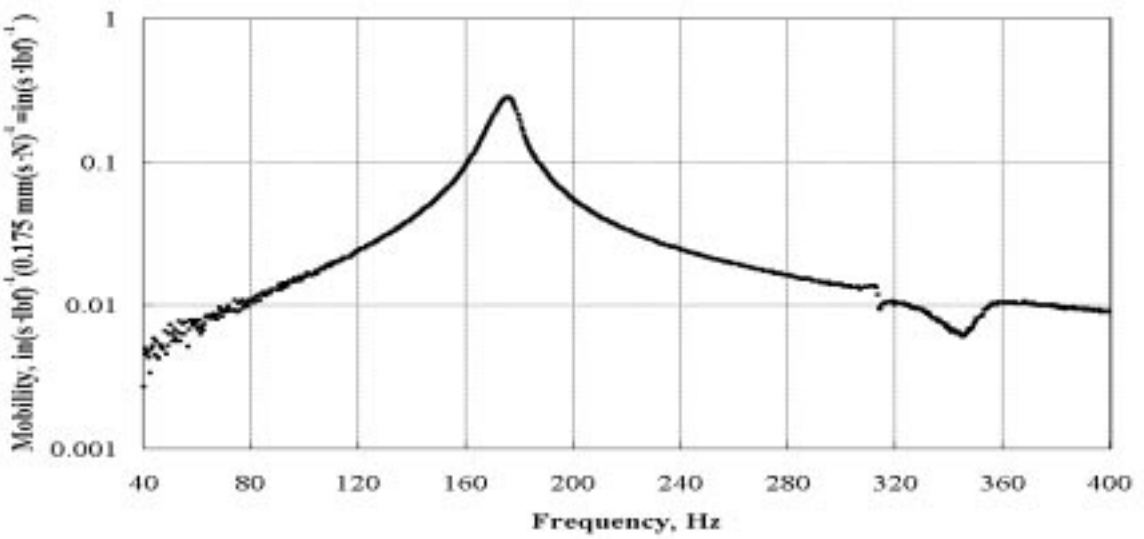

Figure 46. Mobility magnitude for in-plane excitation and response recorded along direction oriented about 5° from test structure *x*-axis

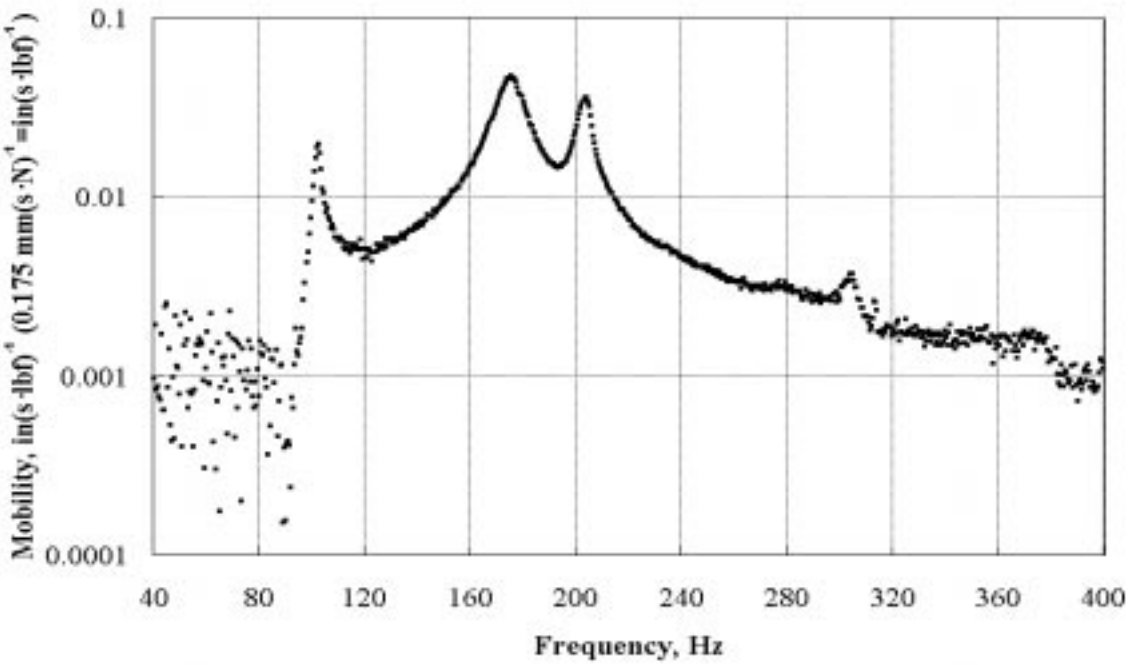

Figure 47. Mobility magnitude for out-of-plane excitation and in-plane response recorded along direction oriented about 5° from test structure *x*-axis

First and second mode motions offset from the principal geometric axes of the test structure were most likely induced by test structure asymmetry. Three reasons account for this asymmetry. First, the boundary conditions at the test stand attachment locations are not symmetric. Therefore, the two boundary conditions possess slightly different stiffness. Second, the columns and braces which comprise the test structure are not perfectly uniform and symmetric. Hence, the columns and braces exhibit mass and stiffness variations. Last, the manner in which the frame was fabricated induced asymmetry. For example, welds between both braces and columns and columns and base plates are not perfectly uniform. Thus, the joints possess slightly different stiffness. Also, some misalignment between the braces and columns most likely exists, although this is not visually apparent.

Since the test structure exhibits first and second motions offset from the principal geometric axes, precise control of test structure motion by the adjustment of an excitation frequency alone is not feasible. Specifically, the precise control of in-plane and out-of-plane motion by adjusting the frequency of an excitation source, such as a shaker, is not feasible. Therefore, below a certain threshold, the amount of out-of-plane motion relative to in-plane motion and vice versa is not easily controlled. Consequently, certain experimental evaluations of ESDM are not feasible with the test structure. For example, the extent to which ESDM can reconstruct very small in-plane velocity components parallel to a surface in the presence of very large out-of-plane components normal to the surface is not easily evaluated since such motion cannot be adequately controlled. However, the existence of first and second mode motions offset from the principal geometric axes did not affect this work since only the ability of ESDM to reconstruct large in-plane velocity components parallel to a surface in the presence of small out-of-plane components transverse to the surface was evaluated. No evaluation of the extent to which ESDM can reconstruct small velocity components parallel to a surface was conducted. Moreover, the ability of ESDM to reconstruct velocity fields with various ratios between velocity components parallel to a surface and transverse to the surface can still be evaluated as long as the ratios do not approach very small values.